Detection of Ridge-like Structures in the Pacific Large Low-Shear-Velocity Province

Nozomu Takeuchi*

Earthquake Research Institute, University of Tokyo, Yayoi 1-1-1, Bunkyo-ku, Tokyo 113-0032, JAPAN

Abstract

Waveform tomography is conducted for SH velocity structures of the entire mantle using approximately 3.5 times the data used for obtaining the previous model, SH18CE. The resultant new model, SH18CEX, exhibits a cluster of ridge-like low-velocity anomalies in the western part of the Pacific Large Low-Shear-Velocity Province (LLSVP). The location of the ridge-like anomalies is in good agreement with the location of the abrupt change in the topography of the D" discontinuity. These results suggest that the LLSVP is associated with a cluster of ridge-like-piles, rather than a single large pile spread over the entire region. The piles probably consist of intrinsically dense material; however, either their volume or density contrast may not be sufficiently large to develop large-scale domes.

Keywords: tomography, Earth's internal structure, lowermost mantle, core-mantle boundary, mantle convection

---

*Corresponding author. Tel.:+81 3 5841 8497; fax: +81 3 3812 9417
Email address: takeuchi@eri.u-tokyo.ac.jp (Nozomu Takeuchi)

1. Introduction

As is well known, there exist two large low-shear-velocity provinces (LLSVPs) in the lowermost mantle beneath the Pacific and Africa. Ridge-like structures (low-velocity anomalies that are horizontally long and narrow) were detected in the African LLSVP via array analyses (e.g., Ni and Helmberger, 2003; Wang and Wen, 2007). Global tomography models also show generally consistent features (e.g., Grand, 2002; Takeuchi, 2007). It is important to verify whether such ridge-like structures are also observed in the Pacific LLSVP; if so, the ridge-like plume can be considered as the fundamental morphology of the upwellings.

Several array analyses were conducted in order to obtain regional structure models for the Pacific LLSVP. For instance, Takeuchi et al. (2008) suggested that the vertical extent of the low-velocity anomalies is approximately 400 km on the western side, whereas He and Wen (2009) suggested that it is approximately 740 and 340 km on the north-western and south-eastern ends, respectively. In these studies, the structure models were obtained by analyzing the data for event-station pairs on, or in the vicinity of, a particular great circle plane. Two-dimensional models were obtained by assuming that the structure is homogeneous in the direction perpendicular to the plane.

However, according to the global tomography model obtained by Schubert et al. (2004), the Pacific LLSVP consists of clusters of small-scale anomalies, and the validity of the aforementioned assumption is not evident. Furthermore, for some regions, such an assumption is clearly invalid; for example, Fig. 4 of Takeuchi and Obara (2010) shows a rapid variation in the ScS-S residuals (~ 8 s variation within 400–500 km) in the direction along which the structures are assumed to be homogeneous by He and Wen (2009). Therefore, further efforts to obtain three-dimensional models are required.

Takeuchi (2007) conducted global waveform tomography using three-dimensional Born kernels and obtained the three-dimensional SH velocity model, SH18CE. The tomography method adopted by Takeuchi (2007) utilizes all the phases in the waveform data (including ScSn and various major and multi-orbit body phases); thus, the resolution of the LLSVPs is improved significantly (see Fig. 2 of Takeuchi, 2007). This method is also advantageous in that it can recover smaller-scale structures by fully considering the finite-frequency effects (see Figs. 3 and 4 of Panning et al., 2009). In this study, we improve the resolution by using a larger data set than that used by Takeuchi (2007) and obtain a three-dimensional SH velocity model of the entire mantle. The obtained model, SH18CEX, exhibits ridge-like low-velocity anomalies in the western part of the Pacific LLSVP, where the resolution of the model is high. In addition, we discuss the plausibility of the obtained features.

2. Data and Method

We invert the transverse component of the broadband waveform data from IRIS GSN and GEOSCOPE for 679 events (Figure 1a). The data set used in this study is a combination of the data set of Takeuchi (2007) (hereafter, referred to as “Data Set 1”) and the new data set (hereafter, refereed to as “Data Set 2”). Data Set 1 includes only data for large events ($M_{\mathrm{W}} \geq 6.5$), whereas Data Set 2 includes data for smaller events (the smallest M_{W} is 6.0). The event distribution for Data Set 2 covers the area that had no or very few events in Data Set 1 (such as Hawaii, the East African rift zone, and mid-ocean ridges). We use a particularly large number of events in the western Pacific region, thereby improving the resolution of the western part of the Pacific LLSVP. The entire data set used in this study consists of $54,790$ traces ($271,798$ time windows), which is approximately 3.5 times the number of traces used by Takeuchi (2007). With the exception of the data set used, the methods and parameters employed in this study are exactly the same as those employed by Takeuchi (2007). The basic information required for further discussion is summarized below.

The periodic ranges of the data set are exactly identical to those of the data set used by Takeuchi (2007). The data set consists of velocity waveforms with three different periodic ranges (200-400 s, 100-200 s, and 50-100). The methods for data selection are exactly identical to those adopted by Takeuchi (2007). We extracted time windows in which the residuals of the phase and the amplitudes between the observed and synthetic seismograms are reasonably small. These data selections were made to avoid the breakdown of the Born approximations used in the inversion in this study. The resultant data set for 200-400 s primarily consists of surface waveform data, whereas the data set for 50-100 s primarily consists of body waveform data.

The model parameters and the damping parameters are also identical to those of Takeuchi (2007). We used the anisotropic PREM (Dziewonski and Anderson, 1981) and the Global CMT solutions as the initial models for the structures and the source parameters, respectively, and we perturbed only the elastic constants (i.e., the other parameters such as density, quality factors, and source parameters were fixed). We expanded the perturbation of the elastic constants N and L (notations follow those of Love, 1927) in terms of 14 radial functions (13 linear spline functions in the mantle and 1 box-car function in the crust) for the vertically dependent part, and spherical harmonics with a maximum angular order of 18 for the horizontally dependent part. We defined the expansion coefficients as the model parameters. Appropriate scaling relations were assumed between the perturbation of N and L. The damping method and parameters are exactly identical to those of Takeuchi (2007). Therefore, we can directly compare the new model, SH18CEX, with the previous model, SH18CE.

3. Obtained Model

3.1. Overall Features, Resolution, and Variance Improvements

The resolution of SH18CEX is considerably better than that of SH18CE (Figure 1b). The resolution of SH18CEX for the western Pacific region is sufficient to recover the checkerboard pattern of heterogeneities whose scale mimics the scale of the structures observed in Fig. 5. Note that the checkerboard patterns exist in both horizontal and vertical directions. The S waves bottoming at various depths should primarily provide the vertical resolution.

The obtained model, SH18CEX, is shown in Figures 2 and 3. First, we compare the lower mantle models of SH18CEX and SH18CE via visual inspection (Figure 2). We see that the overall patterns, i.e., the long-wavelength features, of the two models are nearly invariant, but the significant differences between the models are the relatively small-scale anomalies observed only in SH18CEX (such as the features indicated by the green arrows in Figure 2). This can probably be attributed to the resolution improvement in the new model.

Next, we compute the correlation coefficients between SH18CEX and SH18CE as a function of depth and degree (Figure 4). The correlation coefficients fluctuate among degrees (Fig. 4a) partly because the heterogeneities are very small for some degrees. To clearly observe the overall features of the correlations, we plot the correlation coefficients for each degree bin (degrees 1-3, degrees 4-6, $\cdots$, degrees 16-18) (Fig. 4b). The thick black boxes denote the ranges where the correlation coefficients are less than 0.70. Although we have a few exceptions, we can confirm that the primary ranges with lower correlation coefficients are higher degree components (degrees 16-18) in the lower mantle, showing that the small-scale features in the lower mantle are the primary differences between the models SH18CEX and SH18CE. The lowermost mantle is the region with lower coefficients for a larger degree range (degrees 10-18), and we will discuss their small-scale features in the next subsection.

The newly identified small-scale features appear to be constrained primarily by the body waveforms in Data Set 2. Table 1 summarizes the variance improvements due to SH18CE and SH18CEX. The variance improvement is defined by

$$\left(1-\sum_{i}\frac{\int\left|u_{\text{obs}}^{(i)}(t)-u_{\text{final}}^{(i)}(t)\right|^{2}dt}{\int\left|u_{\text{obs}}^{(i)}(t)-u_{\text{init}}^{(i)}(t)\right|^{2}dt}\right)\times 100\ (\%), \tag{1}$$

where $u_{\text{obs}}^{(i)}$ is the i-th time window of the observed seismograms, and $u_{\text{init}}^{(i)}$ and $u_{\text{final}}^{(i)}$ are the i-th time window of the synthetic seismograms for the initial and the final model (either SH18CE or SH18CEX), respectively. The evaluation of the variance improvements for Data Set 2 required extensive computational resources; hence, we used an approximation. We selected the data for 220 out of 488 events of Data Set 2, and we computed the variance improvements for the selected 220 events. We assumed that these improvements are identical to those for all 488 events of Data Set 2. Note that the event selection was based only on the event date (events between 01/2006 and 09/2007 were selected), and no other selection rules were applied.

SH18CEX exhibits improvements comparable with those of SH18CE for the periodic ranges of 200-400 s and 100-200 s (Table 1, top). For the periodic range of 50-100 s, SH18CEX also exhibits comparable improvements for the existing data (34% for SH18CE and 31% for SH18CEX); on the other hand, it exhibits greater improvements for the incremental data (23% for SH18CE and 31% for SH18CEX) (Table 1, top). Improvements for the incremental data themselves are not surprising because they are included only in the inversion for SH18CEX, but note the larger improvements for the periodic range of 50-100 s compared with the other ranges. Considering that the data set of 50-100 s primarily consists of body waveforms, the results suggest that the incremental constraints on the Earth's structures are primarily attributable to the body waveforms in the incremental data set.

For the periodic range of 200-400 s, the improvements for Data set 1 are greater than those for Data set 2 (e.g., 44% and 32%, respectively, for SH18CEX) (Table 1, top). This is probably due to the fact that the signal-to-noise ratios of Data Set 2 are not adequate for longer periods because Data Set 2 includes data for smaller events. Indeed, for the periodic range of 200-400 s, variance improvements for larger events (Mw ≥ 6.5) are significantly larger than those for the data for smaller events (Mw < 6.5) (38% and 21%, respectively, for SH18CEX) (Table 1, bottom). However, note that this does not hold for the periodic range of 50-100 s (30% and 32%, respectively, for SH18CEX) (Table 1, bottom), which suggests that such problems are not encountered in this periodic range. Therefore, we can conclude that the small-scale features in the lower mantle would be better constrained by the incremental data set.

3.2. Small-Scale Features in the Western Pacific Region

We investigate the small-scale features observed in SH18CEX. We focus on the western Pacific region, where the resolution of SH18CEX was confirmed to be high in Fig. 1b. The enlarged figures (Figure 5, top) indicate that the strong low-velocity anomalies are horizontally long and narrow in the vicinity of the core-mantle boundary (CMB). These ridge-like anomalies surround the relatively high-velocity region (represented by the green dot in Fig. 5), suggesting that the observed strong low-velocity anomalies are associated with the return flow of the downwelling at the center. Such features are not well observed in SH18CE (Figure 5, bottom).

Part of the strong anomalies (those intersected by the line A-A' in Figure 5) extend to the shallower region. The vertical cross sections (Figure 6, top) show that the extent of the anomalies is wide in the NW-SE direction, narrow in the NE-SW direction, and high upwards. These features are similar to those observed in the African LLSVP (e.g., Ni and Helmberger, 2003; Wang and Wen, 2007).

We can confirm some similarities between SH18CEX and several recent models. Figure 6 shows a comparison of SH18CEX, HMSL-S06 (Houser et al., 2008) and S40RTS (Ritsema et al., 2011). In each section of A-A'

(Fig. 6, left), we can confirm tall and wide low-velocity anomalies; however, the anomalies in HMSL-S06 and S40RTS appear to be slightly less tall and slightly less wide, respectively, as compared to those in SH18CEX. In each section of B-B' (Fig. 6, right), we can confirm two piles of low-velocity anomalies. The right pile is taller than the left in each model; however, the pile in SH18CEX appear to be tallest. Therefore, we can say that the ridge-like anomalies are more pronounced in the model obtained in this study.

The observed ridge-like anomalies are not likely to be caused by resolution smearing. Figure 7 shows the resolution kernels for the input anomalies having a point-wise distribution in the horizontal direction. The extents of the input anomalies in the vertical direction are different between Figs. 7a and 7b. The kernels are more or less isotropic in the horizontal direction, and few elongations are observed. Moreover, the smearing in the vertical direction is small. Therefore, we can conclude that the ridge-like anomalies are not due to the smearing effects.

4. Consistency with the Travel Time Data

We confirm the plausibility of the obtained model by checking its consistency with the observed travel time data. We plot the distribution of the ScS-S travel time residuals observed by using Japanese broadband seismic arrays (Figure 8a). $3,469$ residuals were measured between $45.3°$ and $80.7°$ using bandpass-filtered velocity seismograms with corner periods of 3.3 and 100 s. It should be noted that these residuals are independent of the data set used in the waveform tomography in that: (i) the former is data from the regional array, whereas the latter is data from global networks, (ii) the former is relatively short-period data (around 3.3 s), whereas the latter is longer-period data (around 50 s), and (iii) the former is relative travel time data, whereas the latter only contains information regarding absolute travel times.

As in Fig. 4 of Takeuchi and Obara (2010), the measurements in this study indicate an 8 s variation in the residuals within a region of around 400–500 km (at the green line labeled P in Figure 8a of this paper). Although the fluctuations are large, we also observe a variation of around 5 s in the residuals (at the green line labeled Q in Figure 8a); the residuals of north-eastern part are approximately 5 s larger than those of the south-western part. These results intuitively suggest the existence of large velocity gradients in the NE-SW direction. Other regions with relatively abrupt changes in the residuals (R and S in Figure 8a) suggest the existence of velocity gradients in the NW-SE direction. These features are generally consistent with those reported previously (e.g., Fig. 1 of Schubert et al., 2004); however, the features in Figure 8a appear to be clearer. This is probably because the results in Fig. 8a are obtained from a single regional array.

The low-velocity anomalies in SH18CEX effectively explain the observed distribution of the ScS-S residuals (Figure 8b, left; see also Figure 8d, left). By introducing a ridge-like structure, we can explain the abrupt change in the residuals at P, Q, and R in Figures 8a and 8c. We can also explain the abrupt change at S by other low-velocity anomalies in the lowermost mantle. In contrast, SH18CE does not explain the observations (Figures 8b, right and 8d, right). Larger residuals are observed in the region surrounded by the lines P, Q, and R (Figs. 8a and 8c), whereas the model SH18CE predicts smaller residuals (Figs. 8b, right and 8d, right). The results strongly suggest that the low-velocity anomalies in SH18CEX are more plausible than those in SH18CE.

The obtained low-velocity structures have good correlations with the D" topography observed by Takeuchi and Obara (2010), who analyzed *ScS*-*SdS* times for the Fiji-Tonga events. The sampling region extends across the ridge-like structure (Figure 9a). The *ScS*-*S* residuals observed by Takeuchi and Obara (2010) were indeed large at the center of the ridge-like structure, and they linearly decreased with increasing distance from the center (Figure 9b, left). The D" discontinuity was deep at the center, became slightly shallower at the side, and abruptly became very shallow beyond the side of the ridge-like structure (Figure 9b, right). The abrupt jump in the discontinuity suggests that the ridge-like structure is probably associated with a chemically distinct pile (Figure 9c), as discussed by Takeuchi and Obara (2010).

5. Discussion and Implications

In several previous studies, the LLSVPs have been interpreted as isolated piles of intrinsically dense materials (e.g., Ni et al., 2002; Ni and Helmberger, 2003; Wang and Wen, 2007). However, such piles are often expected to have larger-scale structures (e.g., Tackley, 1998, 2002; McNamara and Zhong, 2005), which seems to contradict the cluster of small plumes observed in this study. In contrast, Schubert et al. (2004) proposed that LLSVPs are clusters of isochemical thermal plumes, which seems to contradict the abrupt change in the topography of the D" discontinuity observed in this study. One solution for these contradictions may be as follows: the piles consist of intrinsically dense materials; however, either the volume or the density contrast of the dense materials is small. Under these circumstances, the thermo-chemical plumes are expected to be similar to the isochemical thermal plumes (see, for example, the discussions by Bull et al., 2009).

The morphology of the plumes has long been debated, even for simple Rayleigh-Bénard convections. Bercovici et al. (1989), for example, suggested that the upwellings in the earth-like spherical shells are conduit-like, whereas Houseman (1990) and Yanagisawa and Yamagishi (2005) suggested that the upwellings are sheet-like. The most fundamental difference between these studies is the Rayleigh numbers that were considered. The existence of ridge-like structures suggests that the convection in the lower mantle is as vigorous as that for large Rayleigh numbers (more than, say, 1000 times the critical Rayleigh number).

In the new model, SH18CEX, we see ridge-like structures in both the African LLSVP and the Pacific LLSVP (Figure 2, top). The structures in the African LLSVP are similar to those obtained by Schubert et al. (2004). The results suggest that both the Pacific and the African LLSVPs consist of clusters of chemically distinct piles. It is notable that piles are not spread over the entire region of the LLSVPs, but confined only to the ridge regions. The recent high-P,T elasticity simulation of deep mantle minerals suggests that small volume fractions of mid-ocean ridge basalt (MORB) in the lowermost mantle are sufficient for explaining the amplitude of V_s and V_ϕ anomalies observed in tomographic studies (Tsuchiya, 2011). The ridge-like pile clusters seem to be compatible with this mineralogical interpretation.

Acknowledgments

We thank two anonymous reviewers for their constructive comments. We used an SGI ALTIX4700 installed at the Earthquake Research Institute, University of Tokyo; an HA8000 installed at the Information Technology Center, University of Tokyo; and the Earth Simulator installed at the Japan Agency for Marine-Earth Science and Technology. The broadband data used in Fig. 8a was provided by the National Research Institute for Earth Science and Disaster Prevention, Japan. This research is partially supported by Grants-in-Aid for Scientific Research (Nos. 19104011, 21740323, and 22000003) and by a cooperative research program of the and Earthquake Research Institute (2010-B-03).

References

Bercovici, D., Schubert, G., Glatzmaier, G. A., 1989. Three-dimensional spherical models of convection in the Earth's mantle, Science, 244, 950-955.

Bull, A. L., McNamara, A. K., Ritsema, J., 2009. Synthetic tomography of plume clusters and thermochemical piles, Earth Planet. Sci. Lett., 278, 152-162.

Dziewonski, A. M., Anderson, D. L., 1981. Preliminary reference Earth model, Phys. Earth planet. Int., 25, 297-356.

Grand, S. P., 2002. Mantle shear-wave tomography and the fate of subducted slabs, Phil. Trans. R. Soc. Lond., 360, 2475-2491.

He, Y., Wen, L., 2009. Structural features and shear-velocity structure of the "Pacific Anomaly", J. Geophys. Res., 114, B02309, doi:10.1029/2008JB005814.

Houseman, G. A., 1990. The thermal structure of mantle plumes: axisymmetric or triple-junction?, Geophys. J. Int., 102, 15-24.

Houser, C., Masters, G., Shearer, P., Laske, G., 2008. Shear and compressional velocity models of the mantle from cluster analysis of long-period waveforms, Geophys. J. Int, 174, 195-212.

Love, A. E., 1927, A Treatise on the Mathematical Theory of Elasticity, Cambridge University Press, Cambridge.

McNamara, A.K., Zhong, S., 2005. Thermochemical Structures Beneath Africa and the Pacific Ocean, Nature, 437, 1136-1139.

Ni, S., Tan, E., Gurnis, M., Helmberger, D. V., 2002. Sharp sides to the African superplume, Science, 296, 1850–1852.

Ni, S., Helmberger, D. V., 2003. Seismological constraints on the South African superplume; could be the oldest distinct structure on earth, Earth Planet. Sci. Lett., 206, 119-131.

Panning, M. P., Capdeville, Y., Romanowicz, B. A., 2009. Seismic waveform modelling in a 3-D Earth using the Born approximation: potential shortcomings and a remedy, Geophys. J. Int., 177, 161-178.

Ritsema, J., Deuss, A., van Heijst, H. J., Woodhouse, J. H., 2011. S40RTS: a degree-40 shear-velocity model for the mantle from new Rayleigh wave dispersion, teleseismic traveltime and normal-mode splitting function measurements, Geophys. J. Int., 184, 1223-1236.

Schubert, G., Masters, G., Olson, P., Tackley, P., 2004. Superplumes of plume clusters, Phys. Earth Planet. Int., 146, 147-162.

Tackley, P. J., 1998. Three-dimensional simulations of mantle convection with a thermochemical CMB boundary layer: D", in The Core-Mantle Boundary Region, Geodynamic Ser., vol. 28, edited by M. Gurnis, M. E. Wysession, E. Knittle, and B. A. Buffett, pp. 231-253, AGU, Washington, D.C..

Tackley, P. J., 2002. The strong heterogeneity caused by deep mantle layering., Geochem. Geophys. Geosyst., 3, 1024, doi:10.1029/2001GC000167.

Takeuchi, N., 2007. Whole mantle SH velocity model constrained by waveform inversion based on three-dimensional Born kernels, Geophys. J. Int., 169, 1153-1163.

Takeuchi, N., Morita, Y., Xuyen, N. D., Zung, N. Q., 2008. Extent of the low-velocity region in the lowermost mantle beneath the western Pacific detected by the Vietnamese broadband seismograph array, Geophys. Res. Lett., 35, L05307, doi:10.1029/2008GL033197.

Takeuchi, N., Obara, K., 2010. Fine-scale topography of the D" discontinuity and its correlation to volumetric velocity fluctuations, Phys. Earth Planet. Int., 183, 126-135.

Tsuchiya, T., 2011. Elasticity of subducted basaltic crust at the lower mantle pressures: Insights on the nature of deep mantle heterogeneity Phys. Earth Planet. Int., in press.

Wang, Y., Wen, L., 2007. Geometry and P and S velocity structure of the "African Anomaly", J. Geophys. Res., 112, B05313, doi:10.1029/2006JB004483.

Yanagisawa, T., Yamagishi, Y., 2005. Rayleigh-Bénard convection in spherical shell with infinite Prandtle number at high Rayleigh number, J. Earth Simulator, 4, 11-17.

Table 1: Comparison of variance improvements.

	Data Set 1		Data Set 2	
	SH18CE	SH18CEX	SH18CE	SH18CEX
200-400 s	42 %	44 %	30 %	32 %
100-200 s	41 %	42 %	33 %	37 %
50-100 s	34 %	31 %	23 %	31 %

	Data Set 2 (Mw ≥ 6.5)		Data Set 2 (Mw < 6.5)	
	SH18CE	SH18CEX	SH18CE	SH18CEX
200-400 s	36 %	38 %	20 %	21 %
100-200 s	34 %	38 %	32 %	36 %
50-100 s	21 %	30 %	24 %	32 %

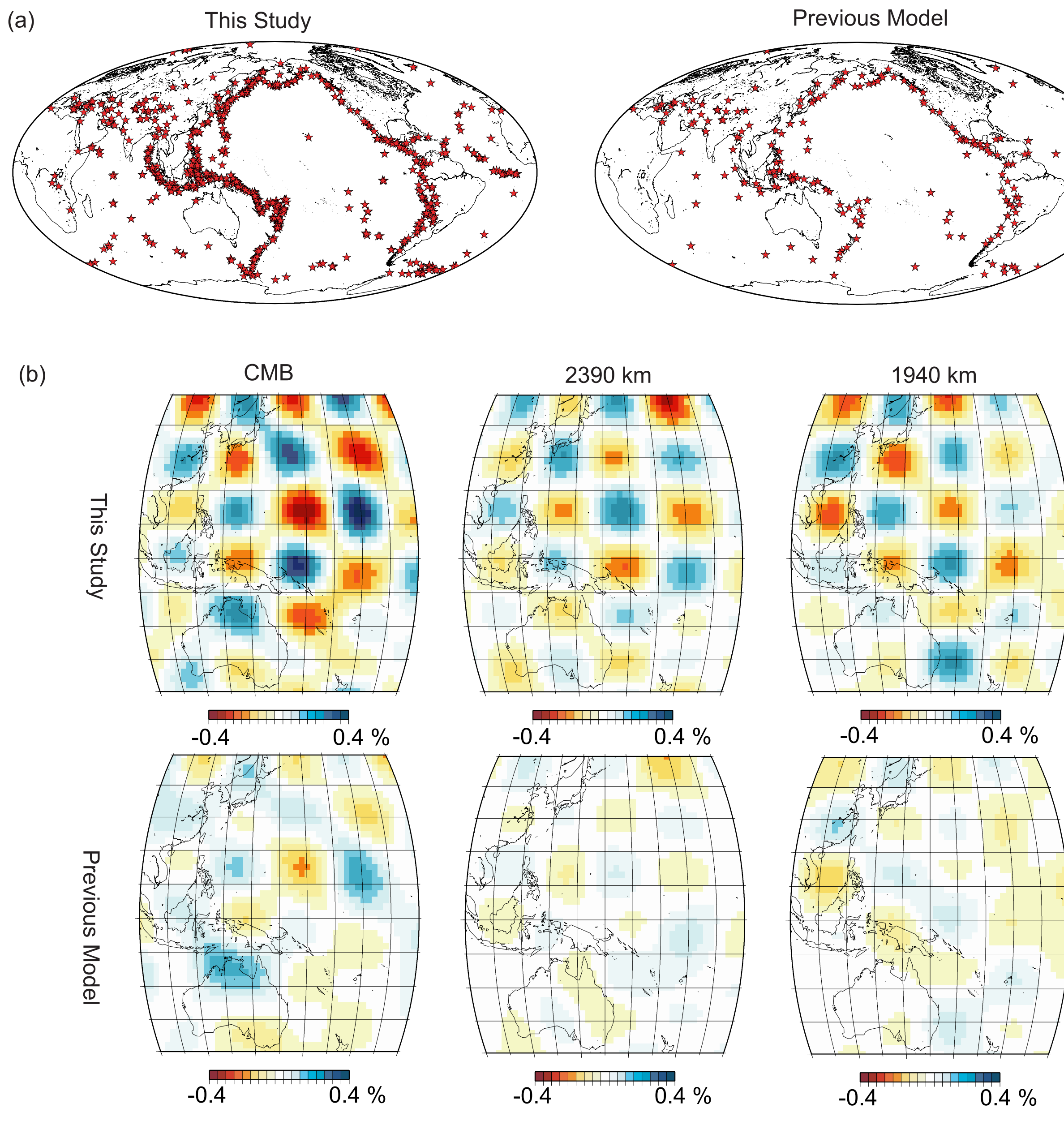

Figure 1: (a) Events used for obtaining SH18CEX in this study (left) and SH18CE (Takeuchi, 2007) (right). (b) Recovered models for checkerboard patterns of the heterogeneities when we use the data sets for SH18CEX (upper figures) and SH18CE (bottom figures).

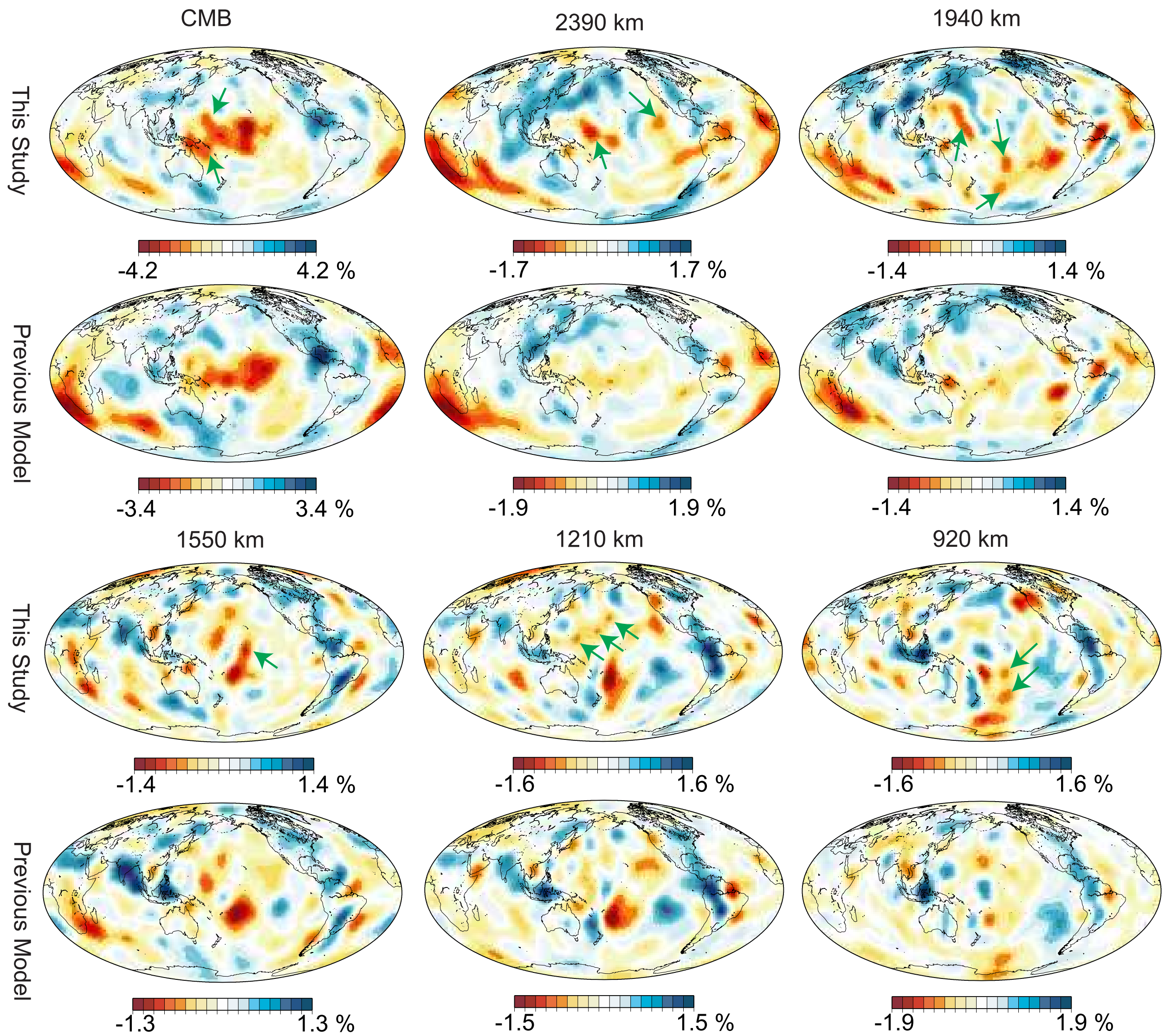

Figure 2: Comparison between SH18CEX (upper figures) and SH18CE (lower figures) at various depths in the lower mantle. The SH velocity perturbations with respect to the initial model, PREM (Dziewonski and Anderson, 1981), are shown. The green arrows indicate examples of the prominent features observed only in SH18CEX.

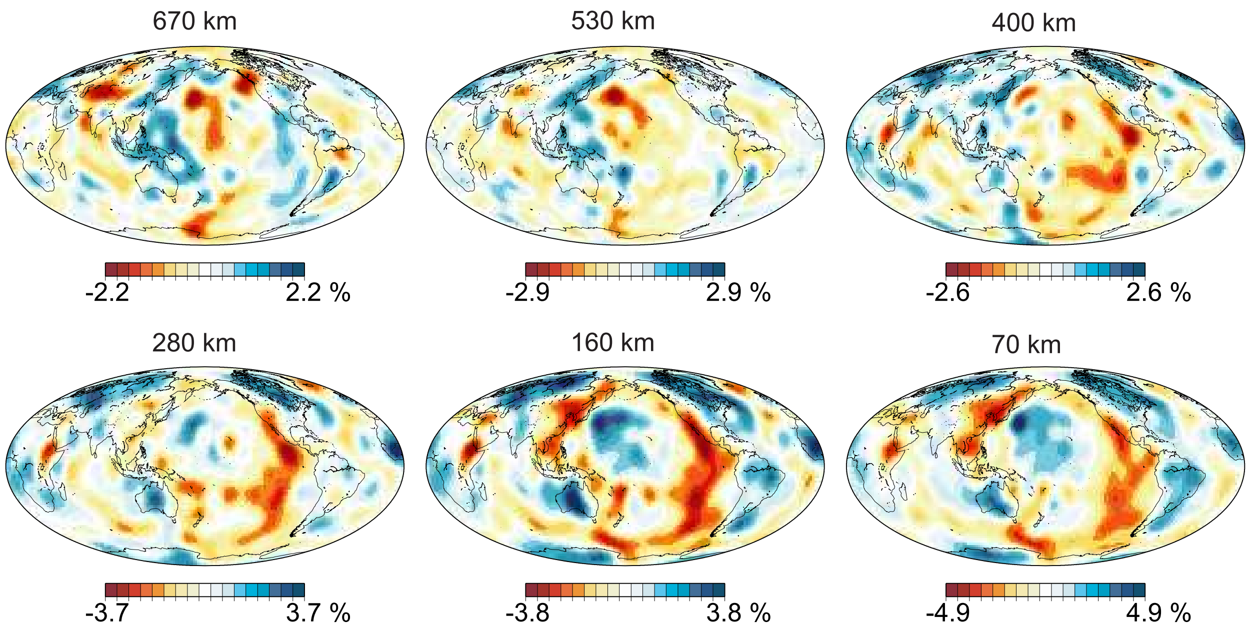

Figure 3: SH18CEX at various depths in the upper mantle.

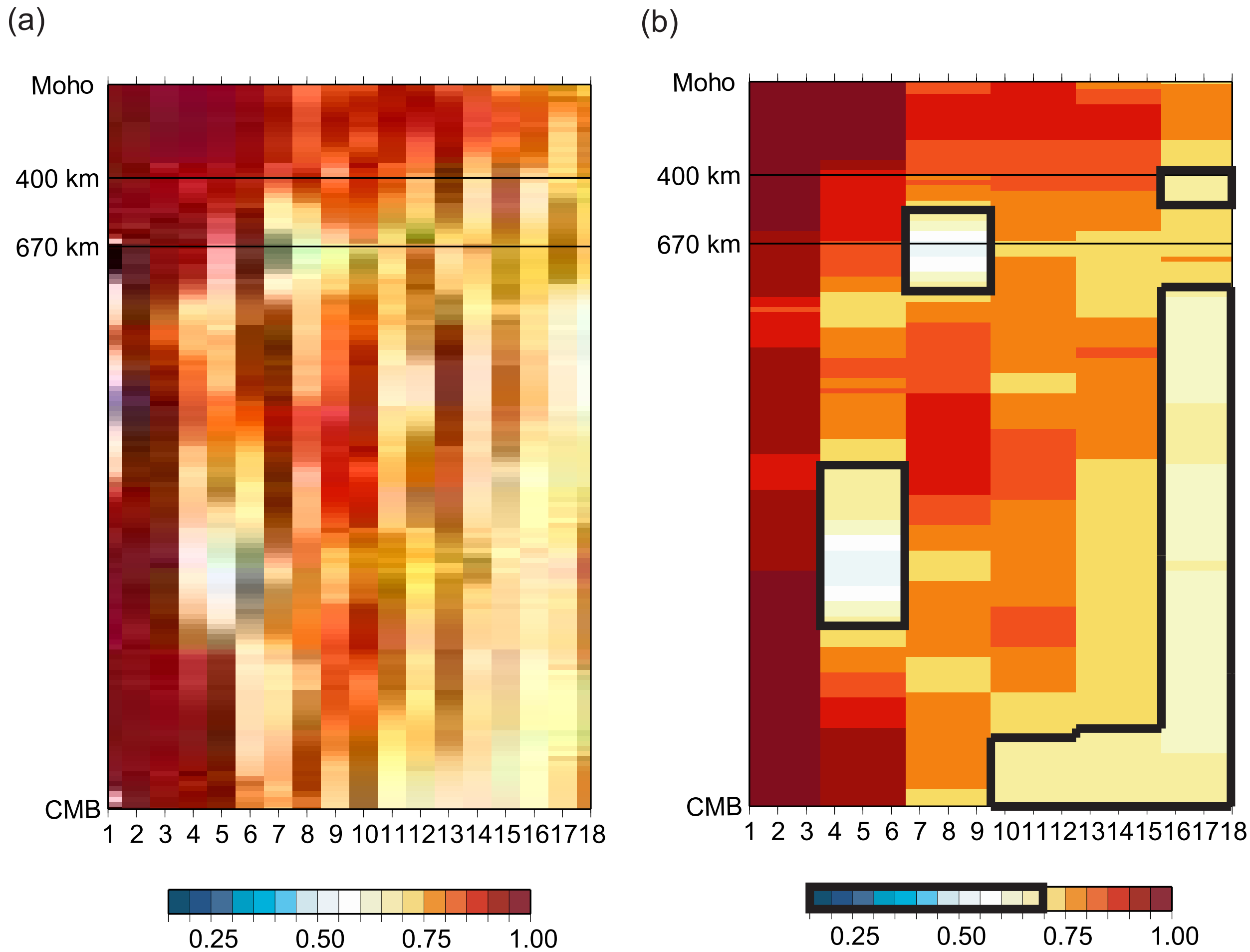

Figure 4: (a) Correlation coefficients between SH18CEX and SH18CE as a function of degree (horizontal axis) and depth (vertical axis). The discontinuities at 400 and 670 km are indicated by solid lines. (b) The same as (a) but showing the correlation coefficients for degree bins (degrees 1-3, 4-6, $\cdots$, 15-18). The thick black boxes denote the regions with correlation coefficients less than 0.70.

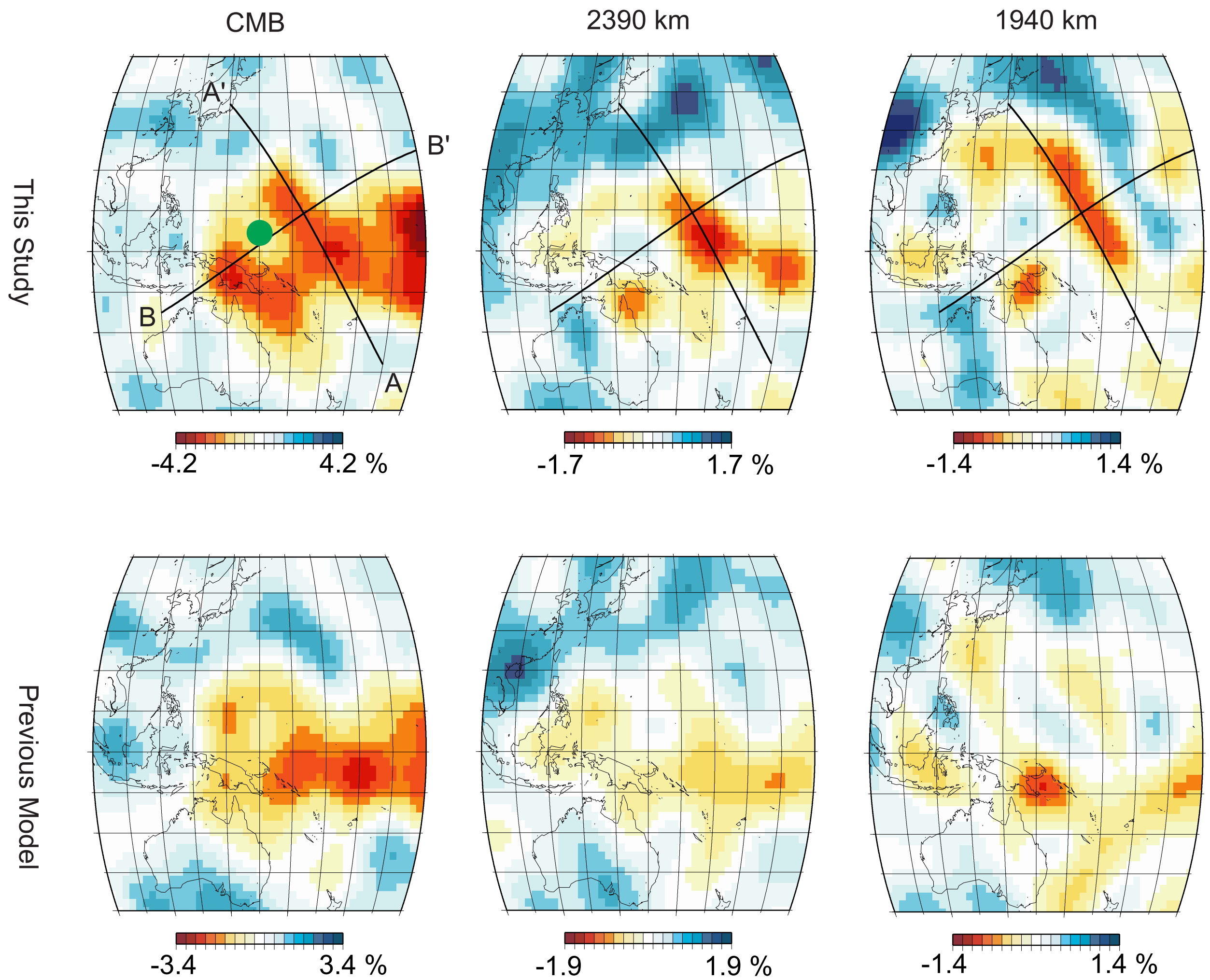

Figure 5: Comparison between SH18CEX (upper figures) and SH18CE (lower figures) in the western Pacific region. The lines A-A' and B-B' denote the locations of the vertical sections shown in Fig. 6. The green dot denotes the relatively high-velocity region discussed in the text.

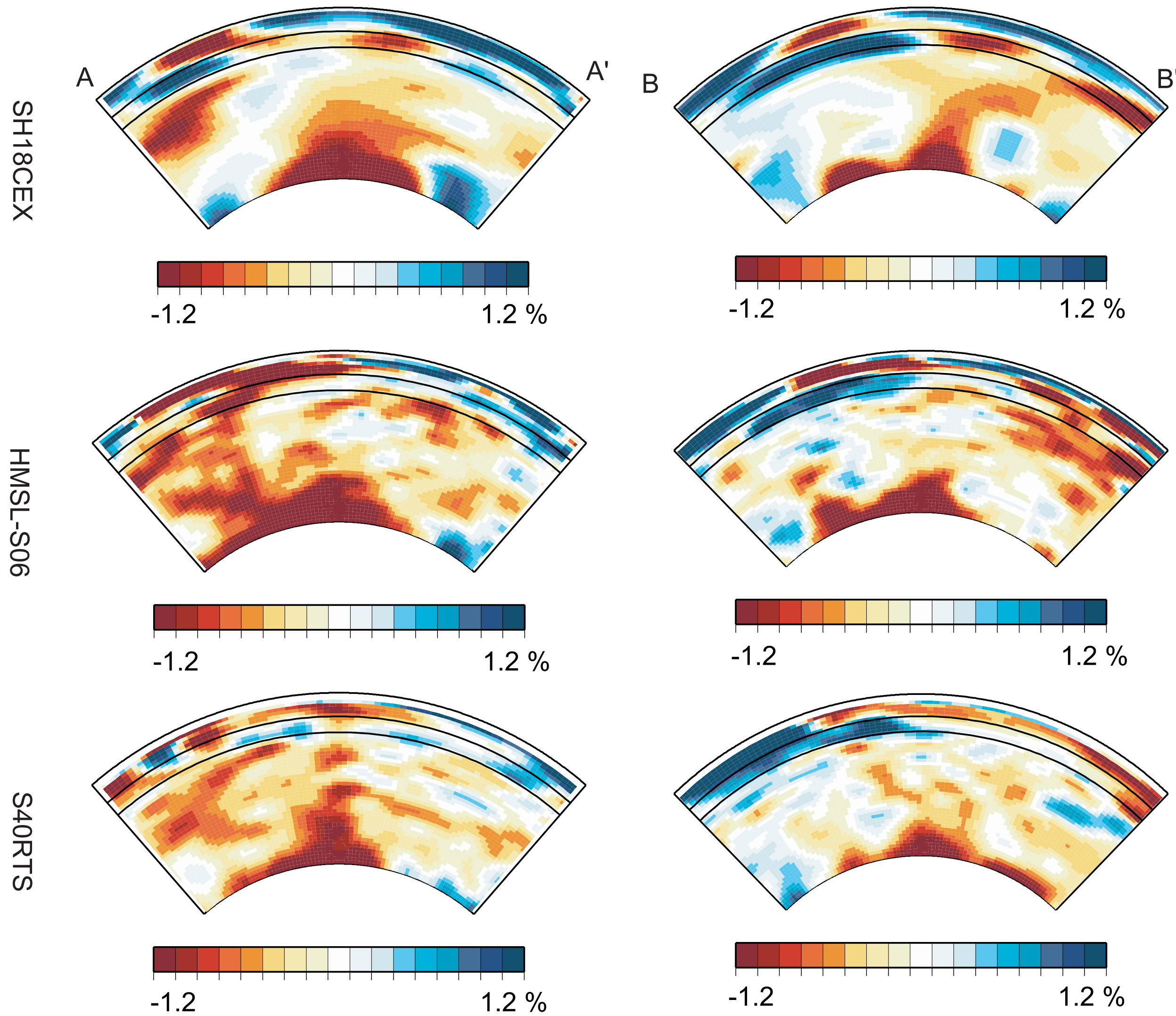

Figure 6: Vertical cross sections of SH18CEX obtained herein (upper figures), of HMSL-S06 obtained by Houser et al. (2008) (middle figures), and of S40RTS obtained by Ritsema et al. (2011) (bottom figures) at the locations indicated by the lines A-A' (left) and B-B' (right) in Fig. 5.

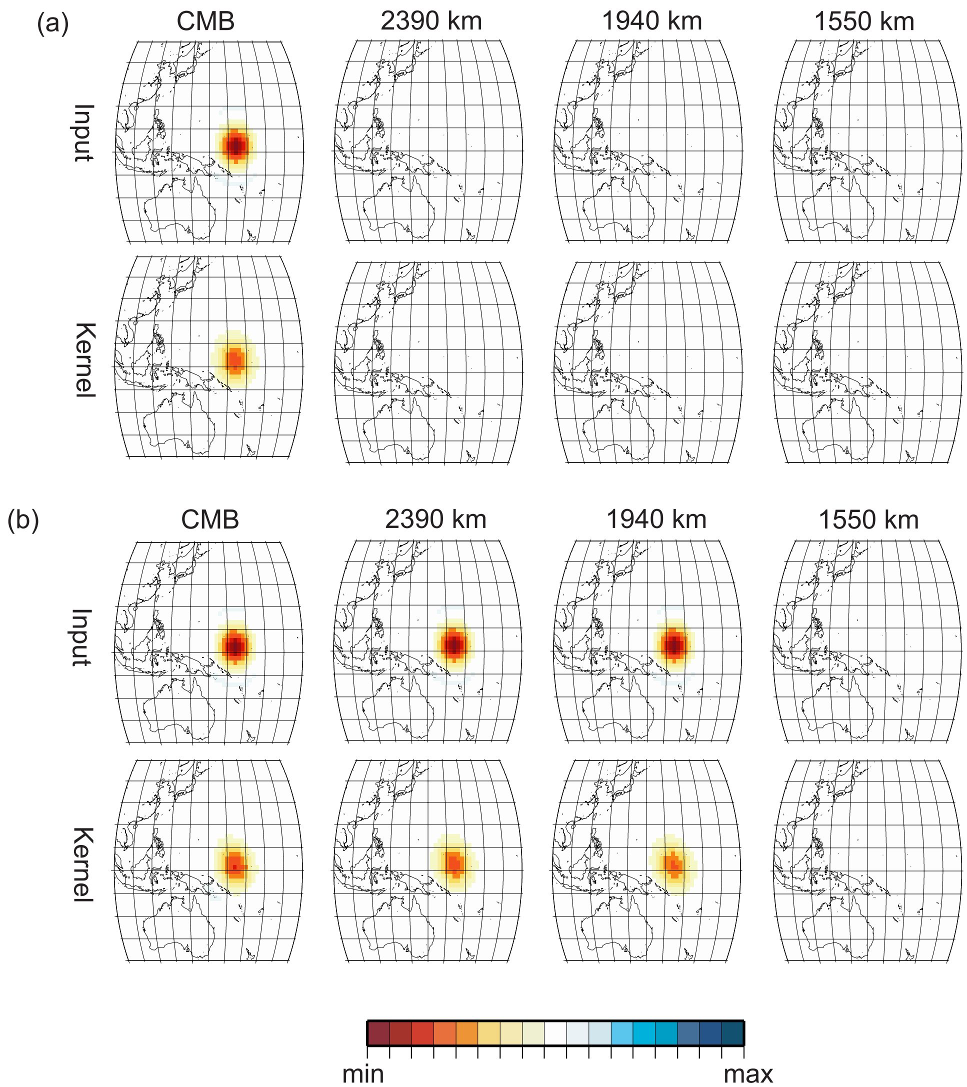

Figure 7: (a)Resolution kernel for low-velocity anomalies having a point-wise distribution in the horizontal direction. The input model (upper figures) and the resolution kernel of SH18CEX (bottom figures) are compared. The vertical dependent part of the input anomalies is given by the perturbations of the model parameters for the linear spline function whose node is at the CMB. (b) The same as (a), except that the input anomalies are given by the perturbations of the model parameters for the linear spline functions whose node is at the CMB, 2390 km depth, and 1940 km depth.

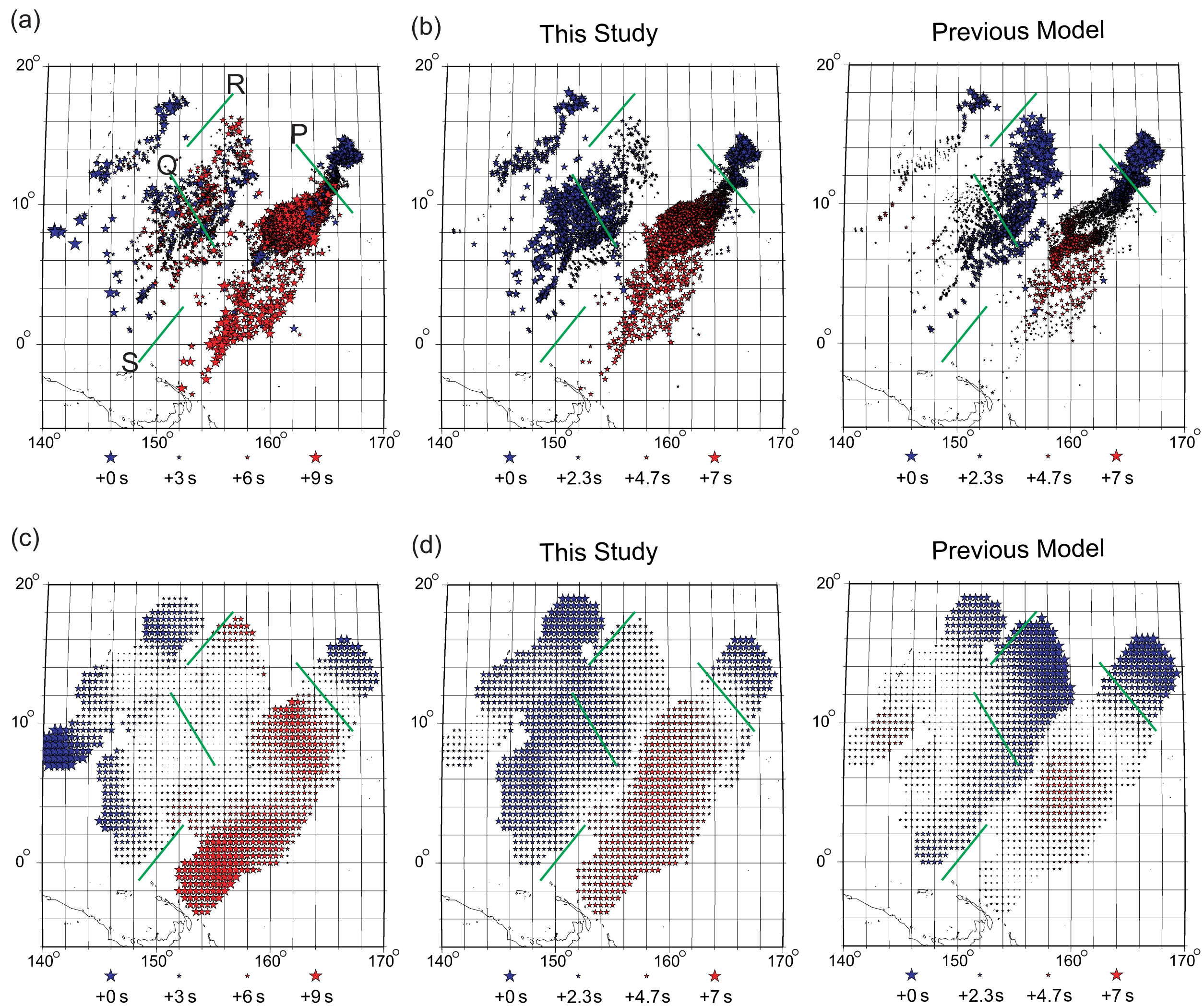

Figure 8: (a) Distribution of the observed ScS-S residuals measured in this study. The residuals are projected at the bouncing point of ScS. The green lines denote the rough locations of the abrupt jump of the residuals discussed in the text. (b) Same as (a), except for the predictions plotted using SH18CEX (left) and SH18CE (right). (c),(d) The same as (a) and (b), respectively, other than plotting the cap averaged residuals with 1.5° radius.

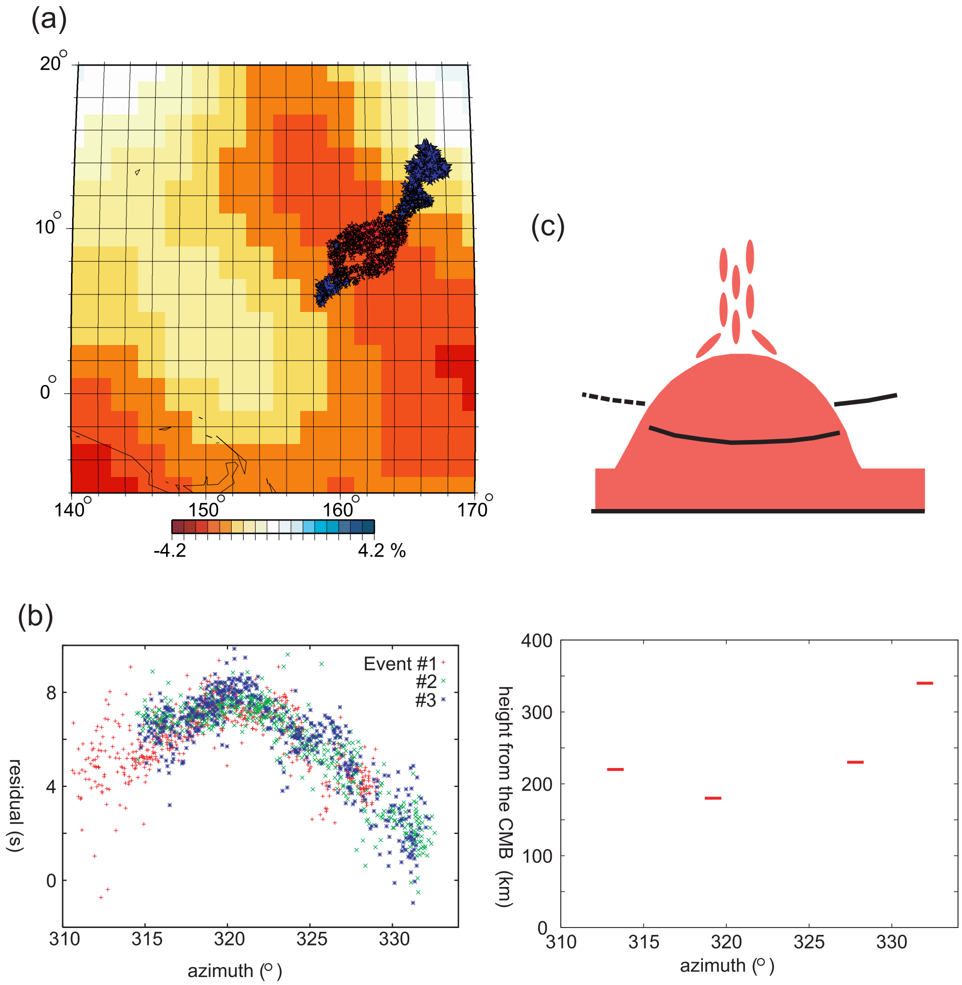

Figure 9: (a) SH18CEX at the CMB overplotted by the *ScS*-*S* residuals previously reported by Takeuchi and Obara (2010). Note that the scale for the residuals is not identical to that in Fig. 8, but it is appropriately chosen for the plot. (b) The *ScS*-*S* residuals shown in (a), plotted as a function of the azimuth. The azimuth is measured from the centroid of the events analyzed by Takeuchi and Obara (2010) (left). The height of the D" discontinuity as a function of the azimuth reported by Takeuchi and Obara (2010) (right). (c) Schematic diagram of the structures of the region studied by Takeuchi and Obara (2010). The red part denotes the chemically distinct region and the solid black lines denote the D" discontinuity.